

Single-parameter quantum charge and spin pumping in armchair graphene nanoribbons

Y. Zhou and M. W. Wu*

*Hefei National Laboratory for Physical Sciences at Microscale and Department of Physics,
University of Science and Technology of China, Hefei, Anhui, 230026, China*

(Dated: March 8, 2013)

We investigate quantum charge and spin pumping in armchair graphene nanoribbons under a single ac gate voltage connected with nonmagnetic/ferromagnetic leads via the nonequilibrium Green's function method. In the case of nonmagnetic leads, where only part of the nanoribbon is subject to an ac gate voltage to break the left-right spatial symmetry, we discover that peaks of the charge pumping current appear at the Fermi energies around the subband edges in the ac-field-free region of the nanoribbon. In the case of ferromagnetic leads with the lead magnetizations being antiparallel to break the left-right symmetry, similar peaks appear in the spin pumping current when the Fermi energies are around the edges of the the majority-spin subbands in the ferromagnetic leads. All these peaks originate from the pronounced symmetry breaking in the transmissions with energies being around the corresponding subband edges. Moreover, we predict a *pure* spin current in the case of ferromagnetic leads with the whole graphene nanoribbon under an ac gate voltage. The ac-field-strength and -frequency dependences of the pumping current are also investigated with the underlying physics revealed.

PACS numbers: 72.80.Vp, 73.23.Ad, 72.25.-b, 72.40.+w

I. INTRODUCTION

Graphene and its lower dimensional cousins, graphene nanoribbons (GNRs) and carbon nanotubes, exhibit abundant new physics and potential applications and hence have attracted much interest in recent years.¹⁻⁸ Among different works in this field, the effect of an ac field on the electrical and optical properties in these materials is one of the main focuses of attention. Many interesting phenomena have been reported, such as the photon-assisted transport,^{9,10} the photovoltaic Hall effect,¹¹ the dynamical Franz-Keldysh effect¹² and the quantum pumping.¹³⁻²⁵

The quantum pumping, which is highly related to the ratchet effect²⁶⁻³⁰ and the photogalvanic effect,³¹⁻³³ describes the generation of a direct current at zero bias in a spatially asymmetric system under ac fields.^{34,35} The quantum pumping of charge and spin currents has been investigated theoretically³⁴⁻⁵⁰ and observed experimentally in semiconductor quantum dots,⁵¹⁻⁵³ quantum wires⁵⁴⁻⁵⁶ and also in carbon nanotubes.¹³ Recently, the quantum charge and spin pumping in GNRs has also aroused growing attention.¹⁴⁻²⁵ Most of these studies focus on the pumping involving more than one time-dependent parameters,¹⁴⁻²² partially because the single-parameter pumping is only possible beyond the adiabatic approximation and thus needs more complex theoretical tool.³⁶ Nevertheless, the single-parameter pumping is more favorable to the application, since the reduction in number of necessary contacts makes the scalable and low-dissipative device more promising.²⁵

So far, there are few investigations on the single-parameter pumping in the GNR. Torres *et al.*²⁵ studied the charge pumping in the ribbon of small size, where

the behaviour is dominated by the resonant tunneling. However, the single-parameter pumping in a typical one-dimensional GNR, i.e., with large length and small width, has not yet been investigated. Moreover, to the best of our knowledge, there is no work on single-parameter spin pumping in this system. The aim of this study is to fill these spaces.

In this paper, we present a detailed study of the single-parameter quantum charge and spin pumping in armchair GNRs contacted with nonmagnetic/ferromagnetic leads via the nonequilibrium Green's function method.⁵⁷ We first address the case of nonmagnetic leads, in which only part of the GNR is subject to an ac gate voltage to break the left-right spatial symmetry. It is discovered that peaks of the negative (positive) charge pumping current appear at the Fermi energies around the energy maximums (minimums) of the subbands in the ac-field-free region of the GNR. Then we turn to the case of ferromagnetic leads with the lead magnetizations being antiparallel in order to break the left-right symmetry. It is shown that a pure spin current can be achieved when the whole GNR is under an ac gate voltage. We also predict peaks in the negative spin pumping current at the Fermi energies around the energy maximums of the majority-spin subbands in the ferromagnetic leads. In the appendix, we discuss the time-dependent ballistic magnetotransport in armchair GNRs contacted with ferromagnetic electrodes and show that the results under the cutoff-energy approximation, artificially introduced by Ding *et al.*,⁵⁸ are qualitatively different from those obtained from the exact calculations.

This paper is organized as follows. In Sec. II, we set up the tight-binding Hamiltonian and the formula of the pumping current. The numerical results are presented in

Sec. III. Finally, we summarize in Sec. IV.

II. MODEL AND FORMALISM

We consider an armchair GNR with a single gate voltage applied between two nonmagnetic/ferromagnetic leads as shown in Fig. 1. In this system, the tight-binding Hamiltonian can be written as

$$H = H_L + H_R + H_g + H_T, \quad (1)$$

in which H_L (H_R) represents the Hamiltonian of the left (right) lead, H_g stands for the Hamiltonian of the GNR and H_T describes the hopping between the GNR and the leads. These terms can be written as

$$H_L = \sum_{i_L, \sigma} E_{L\sigma} c_{i_L, \sigma}^\dagger c_{i_L, \sigma} - \sum_{\langle i_L, j_L \rangle, \sigma} t_{L\sigma} c_{i_L, \sigma}^\dagger c_{j_L, \sigma}, \quad (2)$$

$$H_R = \sum_{i_R, \sigma} (E_{R0} + \sigma M_R \cos \theta) c_{i_R, \sigma}^\dagger c_{i_R, \sigma} + \sum_{i_R, \sigma} M_R \sin \theta c_{i_R, \sigma}^\dagger c_{i_R - \sigma} - \sum_{\langle i_R, j_R \rangle, \sigma} t_{R\sigma} c_{i_R, \sigma}^\dagger c_{j_R, \sigma}, \quad (3)$$

$$H_g = \sum_{i_g, \sigma} V_{i_g} d_{i_g, \sigma}^\dagger d_{i_g, \sigma} - \sum_{\langle i_g, j_g \rangle, \sigma} t_g d_{i_g, \sigma}^\dagger d_{j_g, \sigma}, \quad (4)$$

$$H_T = - \sum_{\alpha=L, R} \sum_{\langle i_\alpha, j_\alpha \rangle, \sigma} t_{T\sigma} d_{i_\alpha, \sigma}^\dagger c_{j_\alpha, \sigma} + \text{H.c.} \quad (5)$$

Here $c_{i_\alpha, \sigma}$ ($d_{i_g, \sigma}$) and $c_{i_\alpha, \sigma}^\dagger$ ($d_{i_g, \sigma}^\dagger$) are the annihilation and creation operators of the electron with spin σ on lattice site i_α (i_g) in the leads (GNR); $\langle i, j \rangle$ denotes pair of nearest neighbors; $E_{\alpha\sigma} = E_{\alpha 0} + \sigma M_\alpha$ are the on-site energy of the spin-up ($\sigma = +$) or spin-down ($\sigma = -$) band in the ferromagnetic leads with $E_{\alpha+} = E_{\alpha-} = E_{\alpha 0}$ for the nonmagnetic leads; θ is the angle between the magnetization directions of right and left leads; $t_{\alpha\sigma}$ and $t_{T\sigma}$ represent the hopping parameters in the leads and between the leads and the GNR, respectively, which are set to be equal to the hopping parameter $t_g = 2.7$ eV in the GNR, unless otherwise specified. The on-site energy of the GNR V_{i_g} takes the values of $V_g + V_{ac} \cos(\Omega t)$ and V_g' in the ac-field-applied and -free regions of the GNR, respectively, with V_{ac} and Ω being the magnitude and frequency of the applied ac gate voltage. Here we apply two static gate voltages V_g and V_g' to modulate the on-site energies in these two regions of the GNR independently to facilitate the identification of the influence of the pumping from different regions.

Exploiting the nonequilibrium Green's function method,⁵⁷ the time-averaged current can be written as (the current flowing from left to right is defined to be

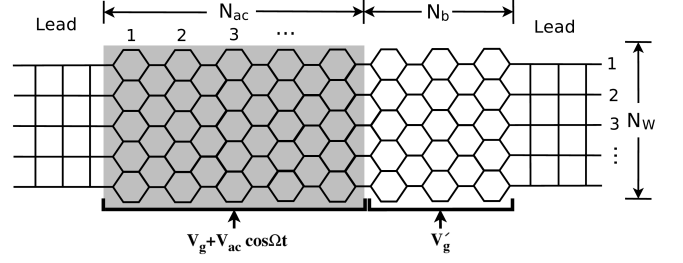


FIG. 1: Schematic view of the armchair GNR connected with two nonmagnetic/ferromagnetic leads.

positive)

$$\bar{I} = \frac{e}{\hbar T_0} \int_0^{T_0} dt \int_{-\infty}^{\infty} \frac{d\varepsilon}{2\pi} \frac{d\varepsilon'}{2\pi} \frac{d\varepsilon_1}{2\pi} e^{i(\varepsilon' - \varepsilon)t} \times \text{Tr} \left\{ \hat{G}^a(\varepsilon, \varepsilon_1) \hat{\Gamma}_R(\varepsilon_1) \hat{G}^r(\varepsilon_1, \varepsilon') \hat{\Gamma}_L(\varepsilon') f_L(\varepsilon') - \hat{G}^a(\varepsilon, \varepsilon_1) \hat{\Gamma}_L(\varepsilon_1) \hat{G}^r(\varepsilon_1, \varepsilon') \hat{\Gamma}_R(\varepsilon') f_R(\varepsilon') \right\}. \quad (6)$$

Here $T_0 = 2\pi/\Omega$; $G^{r(a,<)}(\varepsilon, \varepsilon')$ is the retarded (advanced, lesser) Green's function in the ac-field-applied region of the GNR; $f_\alpha(\varepsilon)$ is the Fermi distribution; $\hat{\Gamma}_\alpha(\varepsilon) = i[\hat{\Sigma}_\alpha^r(\varepsilon) - \hat{\Sigma}_\alpha^a(\varepsilon)]$, with $\Sigma_L^{r(a)}(\varepsilon)$ and $\Sigma_R^{r(a)}(\varepsilon)$ representing the retarded (advanced) self-energies from the left lead and both the right lead and the ac-field-free region of the GNR, respectively. The self-energy has the form

$$\hat{\Sigma}_\alpha^\square = \hat{R}_\alpha \begin{pmatrix} \hat{\Sigma}_{\alpha+}^\square & 0 \\ 0 & \hat{\Sigma}_{\alpha-}^\square \end{pmatrix} \hat{R}_\alpha^\dagger, \quad (7)$$

where $\square = r, a$, the rotational matrix \hat{R}_α is defined as

$$\hat{R}_\alpha = \begin{pmatrix} \cos \frac{\theta_\alpha}{2} & -\sin \frac{\theta_\alpha}{2} \\ \sin \frac{\theta_\alpha}{2} & \cos \frac{\theta_\alpha}{2} \end{pmatrix} \quad (8)$$

with $\theta_L = 0$ and $\theta_R = \theta$.

Then we need to calculate $\hat{G}^r(\varepsilon, \varepsilon')$. It is known that the eigenstates of the isolated GNR with and without an ac gate voltage, labelled as $\Phi(t)$ and $\Phi_0(t)$ respectively, satisfy the relation^{59,60}

$$\Phi(t) = \Phi_0(t) \exp \left\{ -\frac{i}{\hbar} \int_0^t V_{ac} \cos(\Omega t) d\tau \right\}. \quad (9)$$

Thus the Green's Function of the isolated ac-field-applied GNR $\hat{g}^r(\varepsilon, \varepsilon')$ has the form

$$\hat{g}^r(\varepsilon_r + n\Omega, \varepsilon_r' + m\Omega) = 2\pi\delta(\varepsilon_r - \varepsilon_r') \bar{g}^r(\varepsilon_r, n, m), \quad (10)$$

$$\bar{g}^r(\varepsilon_r, n, m) = \sum_N J_{n-N} \left(\frac{V_{ac}}{\Omega} \right) J_{m-N} \left(\frac{V_{ac}}{\Omega} \right) \hat{g}_0^r(\varepsilon_r + N\Omega). \quad (11)$$

In these equations $\varepsilon_r \in [-\frac{\Omega}{2}, \frac{\Omega}{2}]$, $\hat{g}_0^r(\varepsilon)$ is the corresponding Green's function of this GNR without the ac

gate voltage, which can be obtained by the recursive method.⁶¹ From the Dyson equation

$$\hat{G}^r(\varepsilon, \varepsilon') = \hat{g}^r(\varepsilon, \varepsilon') + \int \frac{d\varepsilon_1}{2\pi} \hat{g}^r(\varepsilon, \varepsilon_1) \hat{\Sigma}^r(\varepsilon_1) \hat{G}^r(\varepsilon_1, \varepsilon'), \quad (12)$$

one obtains

$$\hat{G}^r(\varepsilon_r + n\Omega, \varepsilon'_r + m\Omega) = 2\pi\delta(\varepsilon_r - \varepsilon'_r) \bar{G}^r(\varepsilon_r, n, m), \quad (13)$$

where $\bar{G}^r(\varepsilon_r, n, m)$ is determined by

$$\begin{aligned} \bar{G}^r(\varepsilon_r, n, m) &= \bar{g}^r(\varepsilon_r, n, m) + \sum_{n_1} \bar{g}^r(\varepsilon_r, n, n_1) \\ &\quad \times \hat{\Sigma}^r(\varepsilon_r + n_1\Omega) \bar{G}^r(\varepsilon_r, n_1, m). \end{aligned} \quad (14)$$

Substituting Eq. (13) into Eq. (6), \bar{I} can be written as

$$\bar{I} = \frac{e}{h} \sum_{\sigma n} \int_{-\infty}^{\infty} d\varepsilon [T_{LR\sigma}^n(\varepsilon) f_L(\varepsilon) - T_{RL\sigma}^n(\varepsilon) f_R(\varepsilon)], \quad (15)$$

in which

$$\begin{aligned} T_{LR\sigma}^n(\varepsilon) &= \text{Tr} \left\{ \hat{\Gamma}_{L\sigma}(\varepsilon) \bar{G}_{\sigma}^a(\varepsilon, \varepsilon + n\Omega) \hat{\Gamma}_{R\sigma}(\varepsilon + n\Omega) \right. \\ &\quad \left. \times \bar{G}_{\sigma}^r(\varepsilon + n\Omega, \varepsilon) \right\} \end{aligned} \quad (16)$$

is the transmission probability from left to right leads involving the absorption ($n > 0$) or emission ($n < 0$) of $|n|$ photons of electrons with initial energy ε and spin σ . Here we have limited ourselves in the parallel and antiparallel configurations of the electrode magnetizations, and thus the contribution from different spin bands can be calculated separately.

In the spatially asymmetric system, generally speaking $T_{LR\sigma}^n(\varepsilon) \neq T_{RL\sigma}^n(\varepsilon)$. Thus even when the external bias is absent, i.e., $f_L(\varepsilon) = f_R(\varepsilon)$, the time-average current can be nonzero and a pump current emerges. In the zero temperature limit, the pumping current with spin σ is given by

$$I_{\text{pump}}^{\sigma} = \frac{e}{h} \sum_n \int_{-\infty}^{E_F} d\varepsilon [T_{LR\sigma}^n(\varepsilon) - T_{RL\sigma}^n(\varepsilon)], \quad (17)$$

with E_F denotes the Fermi energy. The charge and spin pumping currents are defined as $I_{\text{pump}}^c = I_{\text{pump}}^+ + I_{\text{pump}}^-$ and $I_{\text{pump}}^s = I_{\text{pump}}^+ - I_{\text{pump}}^-$, respectively. Further considering the time-reversal symmetry, one has $T_{LR\sigma}^n(\varepsilon) = T_{RL\sigma}^{-n}(\varepsilon + n\Omega)$. This means that the photon-assisted transmission with the initial and final energies both below the Fermi energy is cancelled by the corresponding one in the opposite direction and hence cannot contribute to the pump current. Consequently, I_{pump}^{σ} can be expressed as

$$I_{\text{pump}}^{\sigma} = \frac{e}{h} \sum_{n>0} \int_{E_F - n\Omega}^{E_F} d\varepsilon [T_{LR\sigma}^n(\varepsilon) - T_{RL\sigma}^n(\varepsilon)]. \quad (18)$$

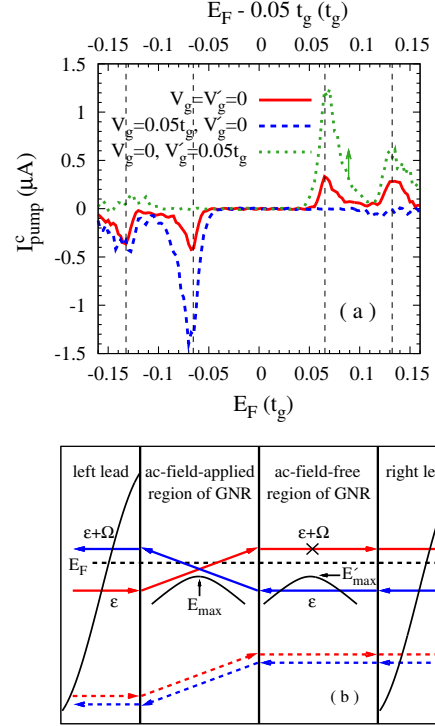


FIG. 2: (Color online) Armchair GNR connected with non-magnetic leads. $N_b = 100$. (a) Charge pumping current as function of the Fermi energy E_F for $V_g = V'_g = 0$ (red solid curve), $V_g = 0.05t_g$, $V'_g = 0$ (blue dashed curve) and $V_g = 0$, $V'_g = 0.05t_g$ (green dotted curve). Note that the scale of E_F for $V_g = 0$ and $V'_g = 0.05t_g$ is on the top of the frame. The vertical black dashed lines indicate the energy maximums and minimums of the subbands in the ac-field-free region of the GNR. (b) The schematic illustration of one peak in the negative pumping current for $V_g = V'_g = 0$. The black dashed line indicates the Fermi energy. The red and blue solid arrows represent the transmissions $T_{LR\sigma}^1(\varepsilon)$ and $T_{LR\sigma}^1(\varepsilon + \Omega)$ in the energy regime satisfying both $E_F - \Omega < \varepsilon < E_F$ and $E'_\text{max} - \Omega < \varepsilon < E'_\text{max}$. The red and blue dashed arrows represent the transmissions $T_{LR\sigma}^1(\varepsilon)$ and $T_{LR\sigma}^1(\varepsilon + \Omega)$ for $\varepsilon < E_F - \Omega$, which cancel each other.

III. NUMERICAL RESULTS

In this section, we present the numerical results of the quantum charge and spin pumping currents in the armchair GNR connected with nonmagnetic/ferromagnetic leads. In our computation, the parameters are chosen to be $N_W = 41$, $N_{ac} = 400$, $V_{ac} = \Omega = 0.01t_g$ and $V_g = V'_g = 0$, unless otherwise specified. Since the width satisfies $N_W = 3M + 2$ with M being an integer number, thus this armchair GNR is metallic.⁶² Also note that the length of the GNR is large enough to totally suppress the contribution from the evanescent modes.⁶³

A. Quantum pumping in armchair GNR connected with nonmagnetic leads

We first study the quantum charge pumping in the armchair GNR connected with nonmagnetic leads, where the on-site energies are chosen to be $E_{\alpha+} = E_{\alpha-} = 0$. We set a finite length of the ac-field-free region of the GNR, i.e., $N_b = 100$, in order to break the symmetry between the transmissions $T_{LR\sigma}^n(\varepsilon)$ and $T_{RL\sigma}^n(\varepsilon)$ and hence induce the pumping current.^{24,25} In Fig. 2(a), we plot the charge pumping current I_{pump}^c against the Fermi energy E_F for $V_g = V'_g = 0$ (red solid curve). Here and hereafter, the energy zero point is chosen to be the Dirac point of the pristine GNR. It is shown that peaks of negative (positive) current appear around the energy maximums (minimums) of the subbands in the GNR indicated by the vertical black dashed lines.

These peaks are understood to originate from the pronounced symmetry breaking in the transmissions with energies around the subband edges in the ac-field-free region. We take one peak in the negative current as an example to illustrate this physics in Fig. 2(b). Here we present the relevant subbands in the ac-field-applied and -free regions of the GNR, whose energy maximums are labelled by E_{max} and E'_{max} , respectively. The relevant subbands in the left and right leads are also shown, in which propagating modes exist in the whole energy range investigated here. The transmissions $T_{RL\sigma}^1(\varepsilon)$ and $T_{LR\sigma}^1(\varepsilon)$ with $E'_{\text{max}} - \Omega < \varepsilon < E'_{\text{max}}$ are plotted in this figure as blue and red solid arrows, respectively. It is seen that the initial (final) energies of these transmissions are lower (higher) than E'_{max} . Although both transmissions are allowed in the ac-field-applied region due to the sideband effect, $T_{LR\sigma}^1(\varepsilon)$ is forbidden in the subband in the ac-field-free region owing to the lack of the propagating modes above E'_{max} . This makes the asymmetry in these transmissions become notable. It is also noted that only for $E_F - \Omega < \varepsilon < E_F$, the single-photon assisted transmissions can contribute to the pumping current as indicated by Eq. (18). As a result, a large negative pumping current appears when $E'_{\text{max}} - \Omega < E_F < E'_{\text{max}} + \Omega$ and reaches its peak value at the Fermi energy around E'_{max} . Similar symmetry breaking can also be found in the multi-photon assisted transmissions. After taking these transmissions into account, the peak of the pumping current appears at almost the same Fermi energy but with wider width. The presence of the peaks in the positive pumping current is based on the similar physics. When the Fermi energy is around the minimum of one subband in the ac-field-free region, this subband only contributes to the transmissions from left to right, but not to the opposite ones. This symmetry breaking leads to the peak of positive current around this minimum.

In order to further verify the above physics, we also plot I_{pump}^c with the modulated on-site energy $V_g = 0.05t_g$, $V'_g = 0$ (blue dashed curve) and $V_g = 0$, $V'_g = 0.05t_g$ (green dotted curve) in Fig. 2(a). It is seen that in the former case, the Fermi energies corresponding to

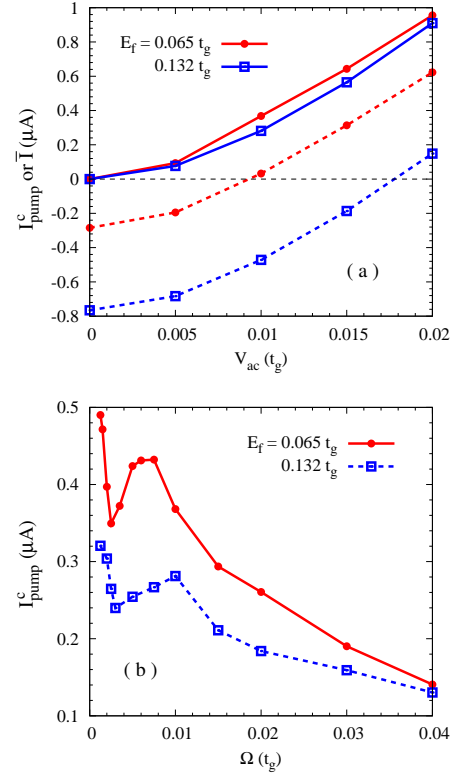


FIG. 3: (Color online) Armchair GNR connected with nonmagnetic leads. $N_b = 100$. (a) Charge current as function of the ac-field strength V_{ac} with the frequency $\Omega = 0.01t_g$ for $E_F = 0.065t_g$ (red curves with \bullet) and $0.132t_g$ (blue curves with \square). The solid and dashed curves represent the currents with no bias (i.e., the pumping current) and negative bias $E_F^L = E_F - \Omega/16$ and $E_F^R = E_F + \Omega/16$. The black dashed line indicates the position of zero current. (b) Charge pumping current as function of the ac-field frequency Ω with $V_{\text{ac}} = 0.01t_g$ for $E_F = 0.065t_g$ (red solid curve with \bullet) and $0.132t_g$ (blue dashed curve with \square).

peaks of negative current are the same as those in the unmodulated case; whereas in the latter one, the Fermi energies corresponding to peaks of positive current are higher than the unmodulated ones by $0.05t_g$. These behaviours agree with the physics discussed above: it is the subband edges in the ac-field-free region that determine the energy range where the pronounced symmetry breaking appears, and hence the Fermi energies corresponding to the peaks in the pumping current. Moreover, the modulation of the on-site energy also brings about more interesting phenomena. It is shown that in the case with $V_g = 0.05t_g$ and $V'_g = 0$ ($V_g = 0$ and $V'_g = 0.05t_g$), the peaks of negative (positive) current appear with larger magnitude than those in the unmodulated case, while all peaks of positive (negative) current disappear. These behaviours for $V_g = 0.05t_g$ and $V'_g = 0$ can be understood as follows. When the Fermi energy is around E'_{max} shown in Fig. 2(b), the relevant transmissions from right to left

in this case are stronger than those without modulation, since the increase of E_{\max} makes more states in the subband in the ac-field-applied region contribute to these transmissions through the sideband effect. Consequently, the asymmetry in the transmissions becomes more pronounced and thus the magnitude of the peak in the negative current becomes larger. On the other hand, when the Fermi energy is around the minimum of one subband in the ac-field-free region, the relevant transmissions in both directions are forbidden in the corresponding subband in the ac-field-applied region, because the energy minimum of this subband is much higher than the related energies of transmissions. This cancels the asymmetry in the transmissions and hence suppresses the peak in the positive current. The behaviours in the case with $V_g = 0$ and $V'_g = 0.05t_g$ can be understood in the similar way.

We stress that the above picture is only valid in the long ribbons, where the energy spectrum can be considered quasi-continuous, but invalid in the short ribbons. In the latter case, the field frequency is smaller than the energy level spacing, thus the behaviour of the pumping current is dominated by the resonant tunneling,²⁵ instead of the physics presented above.

Then we turn to the ac-field-strength and frequency dependences of the pumping current. In Fig. 3(a), the pumping current is plotted against the ac-field strength V_{ac} with frequency $\Omega = 0.01t_g$ for two Fermi energies $E_F = 0.065t_g$ and $0.132t_g$, which correspond to the two peaks of positive current in Fig. 2(a). It is seen that I_{pump}^c increases monotonically with V_{ac} for various Fermi energies. This is because the photon-assisted transmissions are enhanced when the ac field becomes stronger. Besides the pumping currents, i.e., the current with no bias, the currents with negative bias $E_F^L = E_F - \Omega/16$ and $E_F^R = E_F + \Omega/16$ are also plotted in this figure by dashed curves. It is seen that the current is negative in the absence of an ac field. When the ac field is strong enough, the pumping current can surpass the current driven by the negative bias and hence make the net current become positive, i.e., along the direction *opposite* to the external bias.

In Fig. 3(b), we plot the pumping currents against the field frequency Ω with strength $V_{ac} = 0.01t_g$ for Fermi energies $E_F = 0.065t_g$ and $0.132t_g$. It is seen that I_{pump}^c presents a nonmonotonic frequency dependence when $\Omega < V_{ac}$. The scenario is as follows. On one hand, with an increase of the frequency, V_{ac}/Ω decreases and thus the photon-assisted transmissions become weaker. On the other hand, the energy range of the transmissions contributing to the pumping current increases with Ω as shown in Eq. (18). The competition of these two factors leads to the complex frequency dependence. For $\Omega > V_{ac}$, the pumping current is shown to decrease with increasing frequency. This is because the ac field becomes ineffective in exciting photons when frequency is high enough.

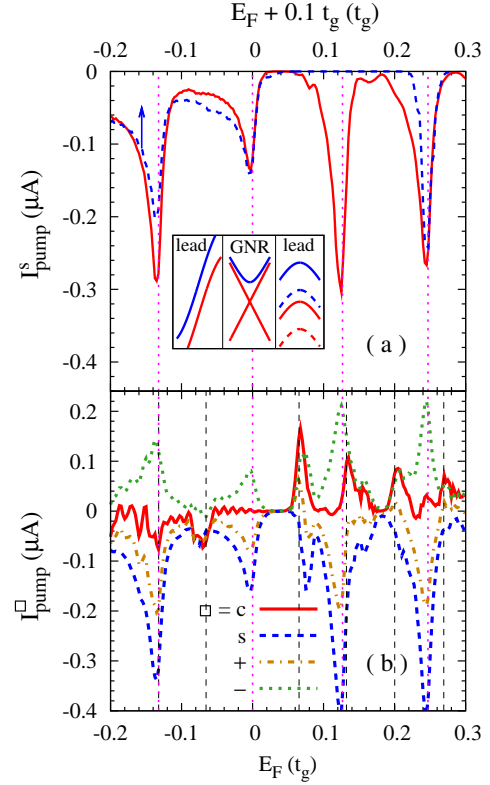


FIG. 4: (Color online) Armchair GNR connected with ferromagnetic leads with the lead magnetizations being antiparallel. (a) Spin pumping current I_{pump}^s as function of the Fermi energy E_F for $E_{L+} = 0$, $E_{R+} = -3t_g$ (red solid curve) and $-3.1t_g$ (blue dashed curve). $N_b = 0$. Note that the scale of E_F for $E_{R+} = -3.1t_g$ is on the top of the frame. In the inset, the spin-up subbands in the GNR and the ferromagnetic leads relevant to the peaks of the pumping current at $E_F = 0$ (red curves) and $0.126t_g$ (blue curves) are schematically plotted. The solid curves represent the subbands in the case with $E_{L+} = 0$ and $E_{R+} = -3t_g$, while the dashed ones in the right panel represent the subbands in the right lead for $E_{R+} = -3.1t_g$. (b) Charge and spin pumping currents together with the spin-up and -down pumping currents against the Fermi energy E_F for $E_{L+} = 0$ and $E_{R+} = -3t_g$. $N_b = 100$. In these figures, the vertical black dashed (pink dotted) lines indicate the energy edges of the subbands in the ac-field-free region of the GNR (the majority-spin subbands in the ferromagnetic leads).

B. Quantum pumping in armchair GNR connected with ferromagnetic leads

Now we investigate the quantum charge and spin pumping in the armchair GNR connected with ferromagnetic leads. In order to break the left-right symmetry, the magnetizations of the two leads are set to be antiparallel, i.e., $E_{L\sigma} = E_{R-\sigma}$, and hence the ac-field-free region of the GNR becomes unessential. We first focus on the case without this region, i.e., $N_b = 0$. In this case, the system satisfies the symmetry $R_\pi \mathcal{R}_{LR}$, where R_π is the spin ro-

tation operator defined by Eq. (8) with rotation angle π and \mathcal{R}_{LR} is the spatial reflection operator in the direction from left to right. Thus, the spin-up and -down pumping currents always satisfy the relation $I_{\text{pump}}^+ = -I_{\text{pump}}^-$. Consequently, the charge pumping current vanishes and a *pure* spin current can be achieved.

We plot the spin pumping current I_{pump}^s for $E_{L+} = 0$ and $E_{R+} = -3t_g$ as red solid curve in Fig. 4(a). It is shown that peaks of negative current appear at the Fermi energies around the maximums of the majority-spin ($L-$ and $R+$) subbands in the ferromagnetic leads, as indicated by the vertical pink dotted lines. In order to reveal the underlying physics, we schematically plot the spin-up subbands in the GNR and the ferromagnetic in the inset of Fig. 4(a). Here only the subbands relevant to the peaks at $E_F = 0$ (red solid curve) and $0.126t_g$ (blue solid curve) are shown. Comparing this inset with Fig. 2(b), one reaches the conclusion that the physics of these peaks is similar to that in the case of nonmagnetic leads: they come from the pronounced asymmetry in the transmissions with energies around the maximums of the majority-spin subbands in the ferromagnetic leads. In order to further verify this physics, we low the on-site energy E_{R+} by $0.1t_g$ and plot the corresponding I_{pump}^s as blue dashed curve in Fig. 4(a). One observes that the Fermi energies corresponding to peaks also decrease by $0.1t_g$ as expected. The only exception is that the peak previously at $E_F = 0.126t_g$ is absent in this case. This feature is based on the similar physics leading to the absence of the corresponding peaks in the case of nonmagnetic leads. As shown in the inset of Fig. 4(a), the energy gap between the subbands relevant to the absent peak in the GNR (blue solid curve in the middle panel) and right lead (blue dashed curve in the right panel) is much larger than the photon energy. Consequently, these subbands cannot contribute to the relevant transmissions in either direction. This leads to the absence of the peak.

Now we turn to the case with finite N_b . Due to the breaking of the symmetry $R_\pi \mathcal{R}_{LR}$, both charge and spin pumping currents can be finite. In Fig. 4(b), we plot these two pumping currents against the Fermi energy for $E_{L+} = 0$ and $E_{R+} = -3t_g$ as red solid and blue dashed curves, respectively. By comparing these results with those in Figs. 2(a) and 4(a), similar features can be seen between the spin or charge pumping currents here and in the case of ferromagnetic leads for $N_b = 0$ or the case of nonmagnetic leads, i.e., peaks in the spin (charge) pumping current appear at the Fermi energies around the edges of the majority-spin subbands in the leads (the subbands in the ac-field-free region of the GNR). The scenario is as follows. Here the pumping current comes from two kinds of symmetry breaking. The first is due to the antiparallel magnetizations of the ferromagnetic leads, which induces peaks where the Fermi energies are around the edges of the majority-spin subbands in the leads, as discussed above. From Fig. 4(b), one further observes that these peaks have similar magnitude but the opposite sign in the spin-up (yellow chain curve) and -down (green dot-

ted curve) pumping currents. This results in peaks in the spin pumping current but provides negligible contributions in the charge pumping current. The second kind of symmetry breaking is from the presence of the ac-field-free region of the GNR, which induces peaks where the Fermi energies are around the subband edges in this region, as demonstrated in Sec. IIIA. These peaks tend to cancel each other in the spin pumping current, but manifest themselves in the charge pumping current. Under the joint effect of these two kinds of symmetry breaking, the behaviour of the spin or charge pumping current resembles that in the case of ferromagnetic leads for $N_b = 0$ or the case of nonmagnetic leads. Moreover, some new features are induced due to the interplay of these two kinds of symmetry breaking, such as the peaks in the negative spin pumping current around $E_F = 0.075t_g$ and the peak in the positive charge pumping current around $E_F = 0.247t_g$. In addition, we verify the ac-field-strength and frequency dependences of the spin and charge pumping currents with ferromagnetic leads resemble those of the charge pumping current with nonmagnetic leads and hence do not repeat here.

IV. SUMMARY AND DISCUSSION

In summary, we have performed a detailed study of the single-parameter quantum charge and spin pumping in the armchair GNR connected with nonmagnetic/ferromagnetic leads via the nonequilibrium Green's function method. We first study the charge pumping in the case of nonmagnetic leads. Here only part of the GNR is subject to an ac gate voltage in order to break the left-right spatial symmetry. We discover that peaks of the negative (positive) charge pumping current appear when the Fermi energies are around the energy maximums (minimums) of the subbands in the ac-field-free region of the GNR. This phenomenon comes from the pronounced symmetry breaking in the transmissions with energies being around these subband edges. We also discuss the pumping current with the modulated on-site energies in ac-field-free and -applied regions of the GNR. Our results show that the Fermi energies corresponding to peaks are influenced by the energy-level shifting in the ac-field-free region, but independent of that in the ac-field-applied region. This is in agreement with the physics presented above. Furthermore, we find that the modulation of the on-site energies also induces the absence of some peaks. This is because the relevant transmissions are forbidden due to the lack of the propagating modes in the corresponding subbands in the ac-field-applied region.

The ac-field-strength and -frequency dependences of the pumping current are also investigated. We show that the pumping current increases monotonically with the ac-field strength due to the enhanced photon-assisted transmissions. Moreover, we discover that at low ac-field frequency, the pumping current exhibits a nonmonotonic

frequency dependence. This is due to the competition of the weakened photon-assisted transmissions and the increasing energy space of the states contributing to the pumping current. At high frequency, the pumping current decreases monotonically with increasing frequency, since the ac field becomes ineffective in exciting photons.

More interesting features are seen in the charge and spin pumping in the case of ferromagnetic leads. Here we set the magnetizations of the two leads to be antiparallel to break the left-right symmetry. In the case with the whole GNR under an ac field, we show that the charge pumping current vanishes and a *pure* spin current can be achieved. We also find that peaks of negative spin pumping current appear at the Fermi energies around the maximums of the majority-spin subbands in the ferromagnetic leads. The physics is similar to the pumping peaks with nonmagnetic leads. In the case with only part of the GNR subject to an ac gate voltage, both the charge and spin pumping currents can be finite. Our calculations show that the behaviour of the spin pumping current is similar to that in the case of ferromagnetic leads with the whole GNR under an ac field, while the behaviour of the charge pumping resemble that with nonmagnetic leads.

Finally, we stress that the main features in the charge and spin pumping currents predicted here do not depend on the specific properties of the leads. Thus they appear not only in the case of the simple-squared-lattice leads used in our model, but also in the case of the other types of leads, e.g., the two-dimensional superlattice^{64,65} and graphene leads. This provides more choices for the experimental investigations.

Acknowledgments

This work was supported by the National Basic Research Program of China under Grant No. 2012CB922002 and the National Natural Science Foundation of China under Grant No. 10725417. Y.Z. would like to thank P. Zhang and H. Tong for their critical reading of this manuscript.

Appendix: Magnetotransport in graphene under ac gate voltage

Recently, Ding *et al.*⁵⁸ studied the magnetotransport of a similar structure, i.e., graphene connected with ferromagnetic leads in the presence of an ac gate voltage. Similar to our model, they treated the transport inside the graphene and leads as the ballistic transport, i.e., without considering any scattering. However, their treatment of the interface between graphene and leads is very different. They neglected the momentum dependence of the coupling matrix and replaced all coupling matrix elements by only one phenomenological parameter. This leads to a divergence in the transmission. To remove the divergence, they artificially introduced a cutoff energy. It

is exactly due to this cutoff energy, many pronounced features in the time-dependent magnetotransport are predicted in that paper.

In the following, we will demonstrate that these pronounced features are just the artificial results induced by the inappropriate treatment of the interface and the introduction of the cutoff energy. Since there is no cutoff energy in our model, we can calculate the transport properties without any approximation used in Ref. 58, and compare the obtained results with corresponding one with the cutoff energy. In the main text of this investigation, the parameters of the ferromagnetic leads are set as $E_{L+} \neq E_{L-}$ and $t_{T\sigma} = t_g$. In this appendix, in order to reveal the problems in that paper more clearly, we change the parameters to $E_{L+} = E_{L-} = 0$ and $t_{T\sigma} = t_g \sqrt{1 + \sigma P}$ with $P = 0.8$ to make $\hat{\Gamma}_{L+}/\hat{\Gamma}_{L-} = (1 + P)/(1 - P)$ as done in Ref. 58. In addition, we only discuss the case with the whole GNR under the ac gate voltage, i.e., $N_b = 0$. Thus for the total transmission $T_{LR/RL}(\varepsilon) = \sum_{\sigma n} T_{LR\sigma/RL\sigma}^n(\varepsilon)$, $T_{LR}(\varepsilon) = T_{RL}(\varepsilon)$ due to the symmetry of this system. The other parameters are set to be $N_W = 80$, $N_{ac} = 400$ and $V_g = 0$.

We first compare the total transmission $T_{LR}(\varepsilon)$ with and without the introduction of the cutoff energy. In Fig. 5(a), we plot $T_{LR}(\varepsilon)$ as function of the energy ε with different ac-field strengths V_{ac} for the field frequency $\Omega = 0.01t_g$ in the parallel configuration of the lead magnetizations.⁶⁶ Here the solid curves represent the results without a cutoff, while the dash ones represent the results from the calculations by replacing Eq. (11) with

$$\begin{aligned} \bar{g}^r(\varepsilon_r, n, m) = & \sum_N J_{n-N}(\frac{V_{ac}}{\Omega}) J_{m-N}(\frac{V_{ac}}{\Omega}) \hat{g}_0^r(\varepsilon_r + N\Omega) \\ & \times \Theta(E_{\text{cut}} - |\varepsilon_r + N\Omega|) \end{aligned} \quad (\text{A.1})$$

with the cutoff energy $E_{\text{cut}} = 0.05t_g$. Our results show that after introducing the cutoff energy in such a way, the field-free transmission is the same as the one without a cutoff when $|\varepsilon| < E_{\text{cut}}$, but becomes zero for $|\varepsilon| > E_{\text{cut}}$.

The difference between the transmissions with and without the cutoff energy becomes more pronounced in the presence of the ac field. In particular, some pronounced peaks appear in the transmissions with the cutoff energy as indicated by the green and blue arrows, which should be absent if calculated properly. This phenomenon can be understood via the Tien-Gordon theory,^{10,59,60,67} which is valid for a weak energy dependence of the self-energy from the leads. This theory gives the formula

$$T_{LR}(\varepsilon) = \sum_m \left[J_m(\frac{V_{ac}}{\Omega}) \right]^2 T_0(\varepsilon + m\Omega), \quad (\text{A.2})$$

where $T_0(\varepsilon) = \text{Tr} \left\{ \hat{\Gamma}_L(\varepsilon) \hat{G}_0^r(\varepsilon) \hat{\Gamma}_R(\varepsilon) \hat{G}_0^a(\varepsilon) \right\}$ is the field-free transmission. The results from this formula are verified to coincide with those from our exact calculations. This theory shows that the field-applied transmission is

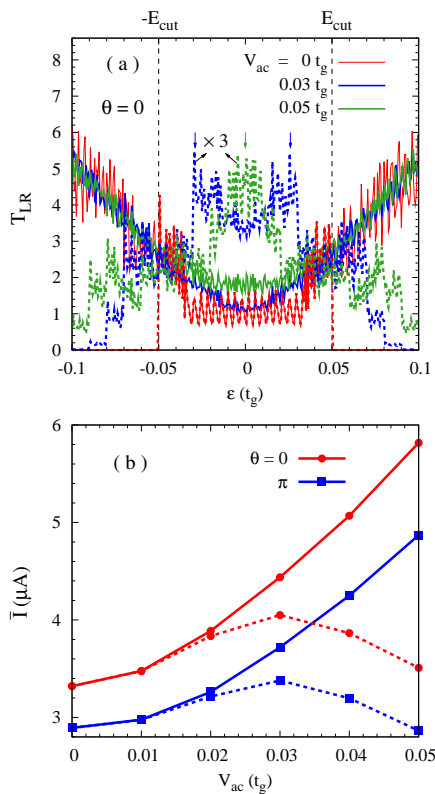


FIG. 5: (Color online) Armchair GNR connected with ferromagnetic leads. (a) Total transmission $T_{LR}(\varepsilon)$ as function of the energy ε with different ac-field strength V_{ac} in the parallel configuration of the lead magnetizations. (b) Time-averaged currents in the parallel and antiparallel configurations as function of the ac-field strength V_{ac} . $\Omega = 0.01 t_g$ in these figures. The dashed curves represent the results with the cutoff energy $E_{cut} = 0.05 t_g$. The blue and green arrows in (a) indicate the positions of the pronounced peaks in the blue and green dashed curves, respectively.

just the weighted average of the field-free transmissions

corresponding to various sidebands. After the cutoff energy is introduced, $T_0(\varepsilon + m\Omega)$ in Eq. (A.2) becomes zero for $|\varepsilon + m\Omega| > E_{cut}$. Thus, the corresponding sidebands cannot contribute to the field-applied transmission. When $|\varepsilon|$ is small, the influence of the cutoff energy is still weak, hence the transmission tends to increase with increasing $|\varepsilon|$ just as the one without a cutoff. Nevertheless, at large $|\varepsilon|$, the influence of the cutoff energy becomes very important. In this case, the transmission tends to decrease with $|\varepsilon|$ due to the absence of the contribution of the sidebands satisfying $|\varepsilon + m\Omega| > E_{cut}$. As a result, the pronounced peaks in the transmission are formed as indicated by the blue arrows. Moreover, when the ac field is strong enough, the decreasing trend from the cutoff energy is always dominant. Thus, the pronounced peak moves to the Dirac point as indicated by the green arrow. Based on the above discussions, one can conclude that this kind of peaks, which also appear in Fig. 2(a) in Ref. 58, are just the artificial results caused by the introduction of the cutoff energy.

Similar problems can be found in the field-strength dependence of the time-averaged current. We plot the time-averaged currents $\bar{I}(\theta)$ in the parallel ($\theta = 0$) and antiparallel ($\theta = \pi$) configurations against the field strength V_{ac} for the Fermi energies $E_F^L = 0.03 t_g$ and $E_F^R = 0$ in Fig. 5(b). It is shown that without a cutoff energy, the currents in both configurations increase monotonically with increasing V_{ac} . This feature is from the increasing weight of the sidebands outside the energy regime between the Fermi energies of two leads, where the field-free transmissions are larger than those inside this energy regime as shown in Fig. 5(a). However, after the introduction of the cutoff energy, the behaviour becomes very different: the currents first increase and then decrease with increasing V_{ac} . The decrease at high V_{ac} is from the increasing weight of the sideband beyond the cutoff energy, where field-free transmission is zero. This means that this decrease, which also appears in Fig. 1(b) in Ref. 58, is an artificial result as well.

* Author to whom correspondence should be addressed; Electronic address: mwwwu@ustc.edu.cn.

- ¹ K. S. Novoselov, A. K. Geim, S. V. Morozov, D. Jiang, Y. Zhang, S. V. Dubonos, I. V. Grigorieva, and A. A. Firsov, *Science* **306**, 666 (2004).
- ² A. K. Geim and K. S. Novoselov, *Nat. Mater.* **6**, 183 (2007).
- ³ A. H. Castro Neto, F. Guinea, N. M. R. Peres, K. S. Novoselov, and A. K. Geim, *Rev. Mod. Phys.* **81**, 109 (2009).
- ⁴ C. W. J. Beenakker, *Rev. Mod. Phys.* **80**, 1337 (2008).
- ⁵ D. S. L. Abergel, V. Apalkov, J. Berashevich, K. Ziegler, and T. Chakraborty, *Adv. Phys.* **59**, 261 (2010).
- ⁶ N. M. R. Peres, *Rev. Mod. Phys.* **82**, 2673 (2010).
- ⁷ E. R. Mucciolo and C. H. Lewenkopf, *J. Phys. Condens. Matter* **22**, 273201 (2010).
- ⁸ S. Das Sarma, S. Adam, E. H. Hwang, and E. Rossi, *Rev.*

- Mod. Phys.* **83**, 407 (2011).
- ⁹ B. Trauzettel, Y. M. Blanter, and A. F. Morpurgo, *Phys. Rev. B* **75**, 035305 (2007).
- ¹⁰ C. G. Rocha, L. E. F. Foa Torres, and G. Cuniberti, *Phys. Rev. B* **81**, 115435 (2010).
- ¹¹ T. Oka and H. Aoki, *Phys. Rev. B* **79**, 081406(R) (2009); *ibid.* **79**, 169901(E) (2009).
- ¹² Y. Zhou and M. W. Wu, *Phys. Rev. B* **83**, 245436 (2011).
- ¹³ P. J. Leek, M. R. Buitelaar, V. I. Talyanskii, C. G. Smith, D. Anderson, G. A. C. Jones, J. Wei, and D. H. Cobden, *Phys. Rev. Lett.* **95**, 256802 (2005).
- ¹⁴ E. Prada, P. San-Jose, and H. Schomerus, *Phys. Rev. B* **80**, 245414 (2009).
- ¹⁵ R. Zhu and H. Chen, *Appl. Phys. Lett.* **95**, 122111 (2009).
- ¹⁶ R. P. Tiwari and M. Blaauboer, *Appl. Phys. Lett.* **97**, 243112 (2010).

- ¹⁷ Z. Wu, J. Li, and K. S. Chan, Phys. Lett. A **376**, 1159 (2012).
- ¹⁸ T. Kaur, L. Arrachea, and N. Sandler, arXiv:1203.3952.
- ¹⁹ R. P. Tiwari and M. Blaauboer, Appl. Phys. Lett. **97**, 243112 (2010).
- ²⁰ E. S. Grichuk and E. A. Manykin, JETP Lett. **93**, 372 (2011).
- ²¹ J.-F. Liu and K. S. Chan, Nanotechnology **22**, 395201 (2011).
- ²² D. Bercioux, D. F. Urban, F. Romeo, and R. Citro, arXiv:1204.5008.
- ²³ Y. Gu, Y. H. Yang, J. Wang, and K. S. Chan, J. Phys. Condens. Matter **21**, 405301 (2009).
- ²⁴ P. San-Jose, E. Prada, S. Kohler, and H. Schomerus, Phys. Rev. B **84**, 155408 (2011).
- ²⁵ L. E. F. Foa Torres, H. L. Calvo, C. G. Rocha, and G. Cunibert, Appl. Phys. Lett. **99**, 092102 (2011).
- ²⁶ F. Jülicher, A. Ajdari, and J. Prost, Rev. Mod. Phys. **69**, 1269 (1997).
- ²⁷ Special issue on *Ratchets and Brownian Motors: Basic Experiments and Applications*, edited by H. Linke, Appl. Phys. A **75**, 167 (2002).
- ²⁸ P. Reimann, Phys. Rep. **361**, 57 (2002).
- ²⁹ P. Hänggi and F. Marchesoni, Rev. Mod. Phys. **81**, 387 (2009).
- ³⁰ E. L. Ivchenko and S. D. Ganichev, JETP Lett. **93**, 673 (2011).
- ³¹ V. I. Belinicher and B. I. Sturman, Sov. Phys. Usp. **23**, 199 (1980).
- ³² E. L. Ivchenko, *Optical Spectroscopy of Semiconductor Nanostructures* (Alpha Science International, Harrow, 2005).
- ³³ S. D. Ganichev and W. Prettl, *Intense Terahertz Excitation of Semiconductors* (Oxford University Press, Oxford, 2006).
- ³⁴ D. J. Thouless, Phys. Rev. B **27**, 6083 (1983).
- ³⁵ B. L. Altshuler and L. I. Glazman, Science **283**, 1864 (1999).
- ³⁶ P. W. Brouwer, Phys. Rev. B **58**, R10135 (1998).
- ³⁷ Y. Levinson, O. Entin-Wohlman, and P. Wölfe, Phys. Rev. Lett. **85**, 634 (2000).
- ³⁸ M. G. Vavilov, V. Ambegaokar, and I. L. Aleiner, Phys. Rev. B **63**, 195313 (2001).
- ³⁹ M. Moskalets and M. Büttiker, Phys. Rev. B **66**, 205320 (2002).
- ⁴⁰ M. Martínez-Mares, C. H. Lewenkopf, and E. R. Mucciolo, Phys. Rev. B **69**, 085301 (2004).
- ⁴¹ V. Kashcheyevs, A. Aharony, and O. Entin-Wohlman, Phys. Rev. B **69**, 195301 (2004).
- ⁴² M. Strass, P. Hänggi, and S. Kohler, Phys. Rev. Lett. **95**, 130601 (2005).
- ⁴³ L. Arrachea, Phys. Rev. B **72**, 121306(R) (2005); L. Arrachea, C. Naón, and M. Salvay, *ibid.* **76**, 165401 (2007).
- ⁴⁴ L. E. F. Foa Torres, Phys. Rev. B **72**, 245339 (2005).
- ⁴⁵ A. Agarwal and D. Sen, Phys. Rev. B **76**, 235316 (2007).
- ⁴⁶ W. Zheng, J. Wu, B. Wang, J. Wang, Q. Sun, and H. Guo, Phys. Rev. B **68**, 113306 (2003).
- ⁴⁷ M. Blaauboer and D. P. DiVincenzo, Phys. Rev. Lett. **95**, 160402 (2005).
- ⁴⁸ K. K. Das, S. Kim, and A. Mizel, Phys. Rev. Lett. **97**, 096602 (2006).
- ⁴⁹ C. Li, Y. Yu, Y. Wei, and J. Wang, Phys. Rev. B **75**, 035312 (2007).
- ⁵⁰ F. Romeo, R. Citro, and M. Marinaro, Phys. Rev. B **78**, 245309 (2008).
- ⁵¹ M. Switkes, C. M. Marcus, K. Campman, and A. C. Gosard, Science **283**, 1905 (1999).
- ⁵² B. Kaestner, C. Leicht, V. Kashcheyevs, K. Pierz, U. Siegner, and H. W. Schumacher, Appl. Phys. Lett. **94**, 012106 (2009).
- ⁵³ S. K. Watson, R. M. Potok, C. M. Marcus, and V. Umansky, Phys. Rev. Lett. **91**, 258301 (2003).
- ⁵⁴ M. D. Blumenthal, B. Kaestner, L. Li, S. Giblin, T. J. B. M. Janssen, M. Pepper, D. Anderson, G. Jones, and D. A. Ritchie, Nat. Phys. **3**, 343 (2007).
- ⁵⁵ B. Kaestner, V. Kashcheyevs, S. Amakawa, M. D. Blumenthal, L. Li, T. J. B. M. Janssen, G. Hein, K. Pierz, T. Weimann, U. Siegner, and H. W. Schumacher, Phys. Rev. B **77**, 153301 (2008); B. Kaestner, V. Kashcheyevs, G. Hein, K. Pierz, U. Siegner, and H. W. Schumacher, Appl. Phys. Lett. **92**, 192106 (2008).
- ⁵⁶ A. Fujiwara, K. Nishiguchi, and Y. Ono, Appl. Phys. Lett. **92**, 042102 (2008).
- ⁵⁷ H. Haug and A.-P. Jauho, *Quantum kinetics in Transport and Optics of Semiconductors* (Springer, Berlin, 2008).
- ⁵⁸ K.-H. Ding, Z.-G. Zhu, and J. Berakdar, Phys. Rev. B **84**, 115433 (2011).
- ⁵⁹ M. Grifoni and P. Hänggi, Phys. Rep. **304**, 229 (1998).
- ⁶⁰ S. Kohler, J. Lehmann, and P. Hänggi, Phys. Rep. **406**, 379 (2005).
- ⁶¹ S. Datta, *Electronic Transport in Mesoscopic Systems* (Cambridge University Press, Cambridge, 1995).
- ⁶² K. Nakada, M. Fujita, G. Dresselhaus, and M. S. Dresselhaus, Phys. Rev. B **54**, 17954 (1996).
- ⁶³ Y. M. Blanter and I. Martin, Phys. Rev. B **76**, 155433 (2007).
- ⁶⁴ R. P. Andres, J. D. Bielefeld, J. I. Henderson, D. B. Janes, V. R. Kolagunta, C. P. Kubiak, W. J. Mahoney, and R. G. Osifchin, Science **273**, 1690 (1996).
- ⁶⁵ P. Kleinert, V. V. Bryskin, Superlattices and Microstruct. **22**, 437 (1997).
- ⁶⁶ The behaviours of the transmissions in the anti-parallel configuration of the lead magnetizations are similar to that in the parallel configuration, and hence not repeated here.
- ⁶⁷ P. K. Tien and J. P. Gordon, Phys. Rev. **129**, 647 (1963).